



HAL
open science

Deciphering the role of faujasite-type zeolites as a cation delivery platform to sustain the functions of MC3T3-E1 pre-osteoblastic cells

Gaëtan Lutzweiler, Yu Zhang, Fanny Gens, Aline Echalar, Guy Ladam, Jérémy Hochart, Théo Janicot, Nadine Mofaddel, Benoît Louis

► To cite this version:

Gaëtan Lutzweiler, Yu Zhang, Fanny Gens, Aline Echalar, Guy Ladam, et al.. Deciphering the role of faujasite-type zeolites as a cation delivery platform to sustain the functions of MC3T3-E1 pre-osteoblastic cells. *Materials Advances*, In press, 10.1039/d2ma00768a . hal-03819764

HAL Id: hal-03819764

<https://hal.science/hal-03819764v1>

Submitted on 18 Oct 2022



HAL is a multi-disciplinary open access archive for the deposit and dissemination of scientific research documents, whether they are published or not. The documents may come from teaching and research institutions in France or abroad, or from public or private research centers.

L'archive ouverte pluridisciplinaire **HAL**, est destinée au dépôt et à la diffusion de documents scientifiques de niveau recherche, publiés ou non, émanant des établissements d'enseignement et de recherche français ou étrangers, des laboratoires publics ou privés.



Cite this: DOI: 10.1039/d2ma00768a

Deciphering the role of faujasite-type zeolites as a cation delivery platform to sustain the functions of MC3T3-E1 pre-osteoblastic cells†

Gaëtan Lutzweiler,^a *^a Yu Zhang,^b Fanny Gens,^a Aline Echalar,^a Guy Ladam,^a Jérémy Hochart,^a Théo Janicot,^a Nadine Mofaddel^c and Benoît Louis ^b

The control of cell fate assisted by synthetic drug-delivering materials is still a challenging task for spatiotemporal regulation of bioactive molecules in native tissues. In this study, the potential of faujasite type (FAU) zeolites for delivering bioactive ions (*i.e.* Ca²⁺ and Mg²⁺) to pre-osteoblastic MC3T3-E1 cells is unveiled. Zeolites are porous aluminosilicates with a large surface area suitable for the storage of biologically active compounds. However, only a few studies have reported the use of zeolites in tissue engineering; therefore, this study aims to correlate the release profile of zeolites with the resulting cell functions. The textural properties of zeolites were assessed *via* MEB, BET, XRF, and EDX analyses. This study shows that either Mg-loaded (Mg-Y) or Ca-loaded (Ca-Y) zeolites are able to gradually release ions over up to three weeks in classical culture media in contrast to the burst release profiles often described in the literature. The ion concentration can be adjusted simply through the mass of zeolite added in the system and was quantified by colorimetric methods and capillary electrophoresis. Three zeolite concentrations were tested (*i.e.* 1, 1.5, and 3 wt%) for both ion types in order to span biologically relevant ranges (from 5.6 to 19.6 mM). The cell responses against various ionic strengths were evaluated not only by the reduction of resazurin assay for viability/proliferation assessment, but also through immunostainings and collagen secretions (Picrosirius red staining). The cell proliferation was found to be proportional to the Ca²⁺ concentration whereas an upper limit seemed to have been reached for Mg 3% compared to Mg 1% and Mg 1.5%. Matrix secretions were delayed under conditions exposed to Ca²⁺ relative to Mg²⁺ after 7 days, but this trend reversed after 21 days. Overall, this study emphasizes the potential role of FAU as a simple, low cost, biocompatible, and versatile way to modulate the functions of MC3T3-E1 cells through ion delivery over up to three weeks. The ion concentration is correlated with the zeolite concentration, and the payload could be easily handled. Thus, this study will make it possible to broaden the applications of zeolites in tissue engineering which can also be implemented in multiple ways including surface coatings and nanocarriers.

Received 29th June 2022,
Accepted 30th August 2022

DOI: 10.1039/d2ma00768a

rsc.li/materials-advances

1. Introduction

In recent years, the resurgence of innovative strategies to treat bone diseases or trauma has shown drastic progress especially with the design of a new generation of biomaterials. Most of the implants used nowadays for bone repair and orthopedics are still made of titanium or ceramics owing to their excellent

resistance against corrosion and good biocompatibility. However, such devices lack osteoconductivity which hampers their regenerative potential,¹ and drove scientists to seek bioactive materials instead, being able to either release chemotactic agents, or implement regeneration with topological or physical cues designed to elicit an appropriate cellular response.²

Regarding bone regeneration, numerous studies have focused on osteogenesis driven by the exposure to growth factors such as bone morphogenic proteins 2 and 7 (BMP-2 and BMP-7), or recombinant human platelet-derived growth factors-BB (rhPDGF-bb),³ though side effects including ectopic bone formation or inflammation could be reported.⁴ Unlike conventional growth factors, smaller molecules including statins or flavonoids could also stimulate bone formation,

^a Normandie Univ, UNIROUEN, INSA Rouen, CNRS, PBS (UMR 6270), 55 rue Saint-Germain, 27000 Évreux, France. E-mail: gaetanlutzweiler@gmail.com

^b ICPEES-UMR 7515, Université de Strasbourg, CNRS, 25 rue Becquerel, F-67087 Strasbourg, France

^c Normandie Univ, UNIROUEN, INSA Rouen, CNRS, COBRA (UMR 6014), 55 rue Saint-Germain, 27000 Évreux, France

† Electronic supplementary information (ESI) available. See DOI: <https://doi.org/10.1039/d2ma00768a>



displaying an intrinsic ability to diffuse through the cell membrane with higher shelf-life.⁵ Importantly, multiple ions including Ca^{2+} , Mg^{2+} , Cu^{2+} and Sr^{2+} appeared as potent and affordable inducers of the differentiation of pre-osteoblastic cells even at low doses, without the stability and conformational-dependence encountered with peptide-derived growth factors.⁶

Among the diverse ions involved in the bone mineralization process and homeostasis, two divalent elements, namely calcium (Ca^{2+}) and magnesium (Mg^{2+}), recur. Indeed, calcium is mostly found within the mineralized matrix of bones in the form of hydroxyapatite (HAp), and is also solubilized in the interstitial fluid, and plays a major role in the mineralization of the extracellular matrix (ECM).⁷ In addition, Ca^{2+} is also known to activate the extracellular signal-related kinase (ERK), subsequently involved in RUNX-2 expression, type I collagen secretion, and osteocalcin upregulation, further promoting the proliferation and differentiation of immature osteoblasts.⁸ Yeh *et al.*⁹ revealed recently that hematopoietic stem cells reside at locations with higher calcium concentrations (~ 1.5 mM) compared to the blood serum, which later affects their clonal expansion. Similarly, magnesium, albeit less abundant, was also shown to contribute to bone mineralization *via* stabilizing effects of amorphous calcium phosphate precursors.¹⁰ The osteoblastic lineage of human bone marrow stromal cells (HBMSCs) could be targeted *via* the release of Mg^{2+} ions activating the Wnt-signaling pathway.¹¹ These ions are usually delivered by biomaterials such as bioceramics, containing calcium phosphates, for instance β -wollastonite¹² or BioGlass[®], which show potential owing to their ability to promote the formation of an apatite layer at the interface with native bones under appropriate calcium concentration conditions.¹³ Equivalently, beta tri-calcium phosphate (β -TCP) is also widely studied as a bone substitute, due to its ability to trigger apatite nucleation upon cell-mediated resorption.¹⁴ For example, Mg^{2+} ions could also be delivered to the surroundings upon resorption of Mg-doped HA, serving as an osteoconductive coating applied onto the surface of titanium implants.¹⁵

However, the release kinetics and consequently the doses must be finely tuned to avoid either a rapid pH variation upon Mg dissolution,¹⁶ or the other associated dysfunctions of bone metabolism.¹⁷ Similarly, vascular calcification can result from high calcium levels in the blood serum.¹⁸ For this purpose, systems that could slow down or regulate the diffusion of manifold ions are highly attractive, for example core-shell microparticles synthesized by Lin *et al.*¹⁹ Indeed, they managed to gradually release Mg for 2 weeks, and a similar trend was observed for the Mg-containing metal organic framework (Mg-MOF-74).²⁰ In another study, Castano *et al.*²¹ generated electrospun fibers made from a bioglass/polymer composite to control the calcium delivery for two weeks.

Porous materials such as clay minerals including the smectite family (*e.g.* montmorillonite and bentonite) are crystalline aluminosilicates and are attractive for drug release applications owing to their large surface area and tunable surface chemistry.^{22,23} Interestingly, zeolite is another class of crystalline aluminosilicates made from connected TO_4 tetrahedra where T denotes either an Al or Si atom, which form a regular

microporous structure during synthesis.²⁴ Zeolites are wide-spread in the industry as catalysts, molecular sieves or sorbents²⁵ since their pore dimensions, surface areas, and sorption capacity can be hierarchized according to the synthesis route.^{26,27} Surprisingly, their application in the biomedical field remains largely under-explored, except scarce reports. Zeolites can be used to produce composite scaffolds intended for tissue engineering, for instance the study by Ninan *et al.*²⁸ reported a gelatin/hyaluronic acid composite loaded with faujasite-type (FAU) zeolites, and highlighted that the oxygen supply to cells was improved after desorption from the FAU cavities. Y-zeolites/Hap composites were also obtained from microwave-assisted precipitation, providing scaffolds which sustain the functions of osteoblastic cells. This method appeared as a versatile tool to modify the surface topology by changing the zeolite percentage.²⁹ MFI-type zeolites are also quite stable in the biological environment (*e.g.* resistance against corrosion) and can be crystallized directly atop some surfaces by *in situ* crystallization which allows the crystalline structure of zeolites to be preserved. Likewise, MFI-coated titanium surfaces led to the reduction of the leaching out of toxic Al and V ions underneath, and enhanced cellular tethering.³⁰ Hence, the surface features such as roughness can therefore be adjusted through zeolite coatings, and, in turn, promote the adhesion and differentiation of osteoblasts.³¹ More recently, nanosized zeolites were also synthesized for the local delivery of gadolinium and carbogen for tumor imaging and treatment in primates,³² but larger molecules such as cyclophosphamide could also be loaded in their channels.³³ Regarding bone tissue engineering, the release of zinc ions on MC3T3-E1 pre-osteoblastic cells, from a zeolitic imidazole framework-8, *i.e.* a hybrid between zeolites and metal organic frameworks (MOFs), was described, and the authors concluded that the biological activity was dose-dependent.³⁴

Considering the unique architectural features of zeolites (*i.e.*, large surface area and hierarchized pore size), and the fact that these materials can be implemented in multiple ways including as nanocarriers,³² or as surface coatings,^{34–36} particular attention can be paid to their use in bone regeneration, which requires establishing their potential action towards bone cells.

Herein, we addressed the role of FAU zeolites as a reservoir to ensure a gradual release with a controlled dosage of two biologically relevant cations, namely calcium and magnesium. The ion release profile was defined, and considered in light of the biological response induced on MC3T3-E1 osteoblastic cells, which encompassed cell morphology, proliferation and collagen secretion.

2. Results and discussion

Both Mg- and Ca-activated zeolites (Mg-USY and Ca-USY) were characterized in order to correlate any biological effect due to their loading/release capacity. These materials exhibited a characteristic pyramidal morphology according to the SEM micrograph shown in Fig. 1(a). Individual crystals were about 0.7–1 μm in size and were aggregated into larger, 5–10 μm



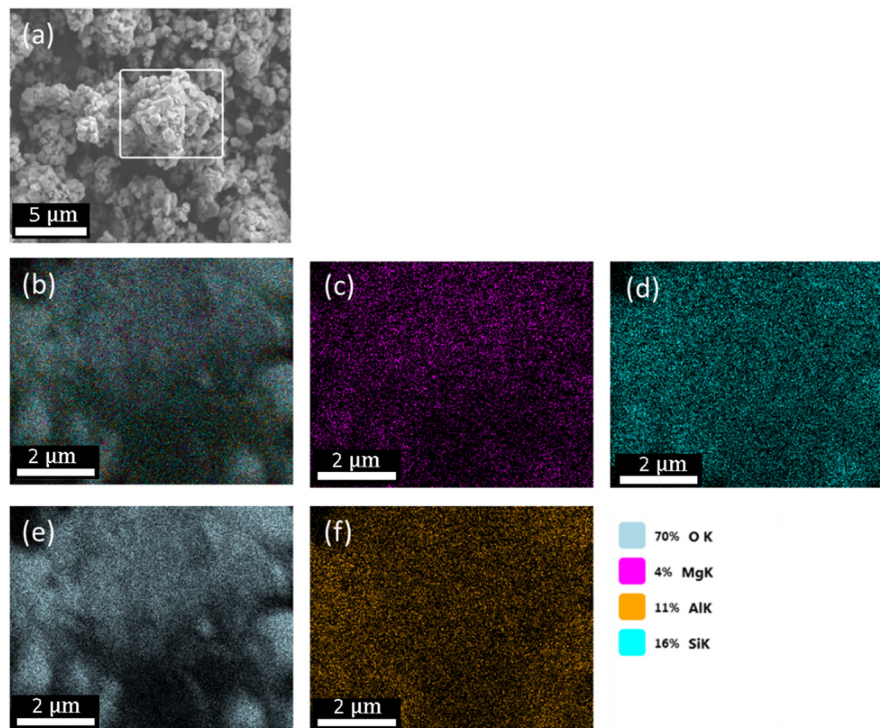


Fig. 1 Image taken by SEM depicting the morphology of FAU nanocrystals (a). The framed area was subjected to elemental analysis to determine the overall atomic composition (b), and the individual percentages of Mg (c), Si (d), O (e) and Al (f).

structures. For this reason, zeolites were placed in culture inserts rather than directly in contact with cells in order to prevent any potential damage resulting from the sedimentation of zeolite aggregates. Moreover, as the purpose of this study was to investigate the potential of FAU zeolites to induce an ion-based modulation of MC3T3-E1 pre-osteoblasts, any cellular response that could arise from direct contact with zeolites should be avoided. The adsorption of Mg ions was confirmed first by elemental EDX analysis (Fig. 1(b) and (c)), showing a homogenous distribution of Mg ions throughout the zeolite

framework, with an atomic percentage estimated around 4% of the whole composition comprising oxygen, aluminum, and silicon (Fig. 1(b)–(e)). Likewise, calcium was also homogeneously distributed within the zeolite crystals (data not shown). One can observe from the N_2 adsorption–desorption experiments a classical type IV isotherm for both Mg- and Ca-loaded FAU (denoted as Mg-Y and Ca-Y in Fig. 2(a), respectively) due to the presence of a hysteresis, which ascertains the coexistence of both micropores and mesopores. The presence of small mesopores (*i.e.* 2–3 nm) was a result of the dealumination process,

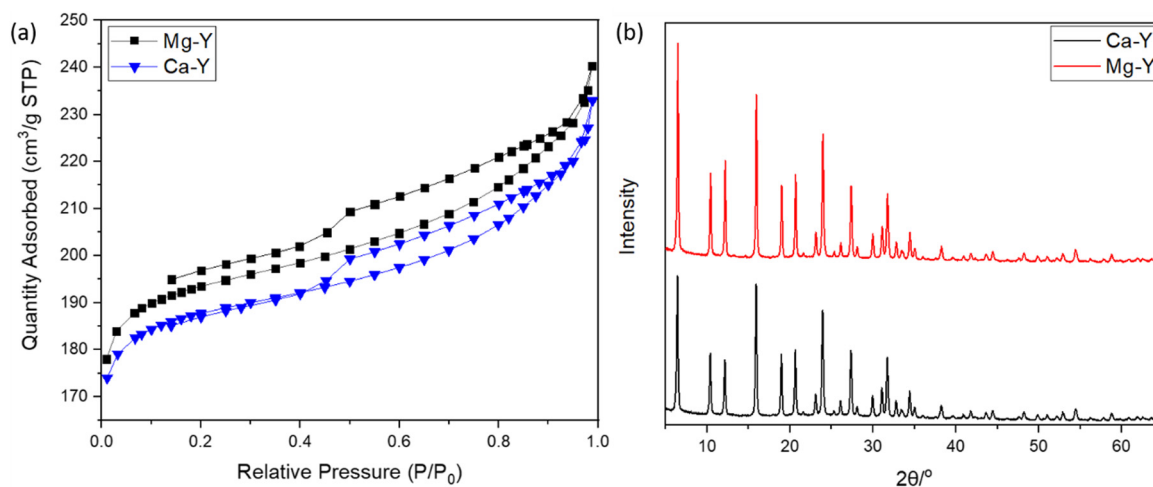


Fig. 2 (a) N_2 adsorption–desorption isotherms of Mg-exchanged FAU (Mg-Y) and Ca-exchanged FAU (Ca-Y). (b) Diffraction patterns of Ca- and Mg-exchanged FAU.



and hierarchically organized micro-mesoporous zeolites were produced.³⁷ Of note, this multiscale porosity can be used to load both bioactive ions and small molecules even though the latter aspect is beyond the scope of this study.

The Mg-Y curve is shifted upward with respect to the Ca-Y curve, which indicates that the loading of Mg ions in the zeolite crystal was less important than for Ca-Y.

Van Mao *et al.*³⁸ already reported that the ability of FAU zeolites (X- and Y-types) to exchange Mg²⁺ ions was less efficient than that to exchange Ca²⁺ ions, which was explained by the higher solvation degree of Mg, leading to larger complexes, and thus limiting the diffusion of these ions throughout zeolite channels. Moreover, Coker *et al.*³⁹ also compared the diffusivity difference between Mg²⁺ and Ca²⁺ ions to the degree of the crystallinity of zeolites, but this argument could be discarded in our case since the XRD patterns of both Mg-Y and Ca-Y were nearly identical (Fig. 2(b)); hence, no structural modification was expected after our soft cation-exchange procedure. Though Mg²⁺ ions are significantly less concentrated in the culture medium (α -MEM) (*i.e.* 0.8 mM for Mg vs. 1.8 mM for Ca), the extent of Mg loading in the zeolite framework may still be large enough to induce a biological response.

The textural properties including the BET surface areas and microporous volumes are presented in Table 1. The amount of ions that can be stored in the zeolite structure is fairly correlated with the quantity of aluminum atoms present in a tetrahedral configuration, whose excess of negative charges is neutralized by compensating cations. The silica-to-aluminum ratio (Si/Al) was estimated to be 2.9 by energy-dispersive X-ray (EDX) (Fig. S1, ESI[†]) analysis, which is in agreement with the common values found for FAU.⁴⁰ X-Ray fluorescence spectroscopy was also performed to obtain a global elemental composition of the solids. A Si/Al = 3.3 was confirmed, being in line with the EDX mapping analysis. More importantly, the Ca and Mg loadings were estimated to be 2.93 and 2.29 wt%, respectively. The cationic exchange in the FAU zeolites could therefore be calculated for Ca-Y and Mg-Y, being 48 and 39%, respectively. These results indicate a higher exchange of Ca²⁺ cations with respect to Mg²⁺-loaded Y zeolites, which is in line with the early studies from Breck.⁴¹

The ion release profile was established in order to determine the kinetics, and the concentrations of either Ca²⁺ and Mg²⁺ ions which can be delivered by the zeolites in the surroundings (Fig. 3(a) and (c)). Therefore, 100, 150 and 300 mg of Ca- and Mg-exchanged FAU were placed at the bottom of 15 mL tubes, being subsequently filled with 10 mL of complete α -MEM media to obtain solutions with 1, 1.5 and 3 wt% of zeolites, respectively. The samples were denoted as X Y%, where X stands for the metal ion (Ca or Mg), and Y is the weight

percentage of zeolites. The ion release studies were performed for 21 days and at 37 °C to be consistent with cell culture experiments. The Mg²⁺ concentration was found to increase gradually over time for 14 days under all conditions, prior to level off, whilst the Ca²⁺ concentration reached a plateau already after 7 days. These results are analogous to the kinetic profile described by Lateef *et al.*,⁴² whose complete Mg²⁺ and Ca²⁺ delivery from nanosized zeolites was reached within the same delay. At each time-point, ion concentrations increased with the amount of zeolites; after 24 h, the concentrations of Ca²⁺ ions were 13.2, 16.6 and 20.6 mM for conditions with 1, 1.5 and 3 wt% of Ca-exchanged FAU, respectively (Fig. 3(d)). After 21 days, these values increased to 18.6, 19.9 and 28.2 mM, corresponding to increases of 36.6% (Ca 1%), 19.8% (Ca 1.5%) and 36.9% (Ca 3%), respectively.

Considering magnesium ions, the measured concentrations after 24 h were 3.9, 5.1 and 7.8 mM following the increasing order of zeolite concentrations. After 21 days, ion levels also increased to 6.7, 7.3 and 14.5 mM, consisting of 71.7% (Mg 1%), 69.8% (Mg 1.5%) and 85.9% (Mg 3%) increases (Fig. 3(a)). This slow cation release kinetics shows a quite different trend from the results presented in the work of Chen *et al.*,⁴³ who found that the release profile of nanosized FAU exchanged with zinc, copper and iron ions, exhibited a plateau at around 1.5 h. Such a discrepancy can be explained by the fact that even if the diffusivity of both Ca²⁺ and Mg²⁺ ions should be enhanced by the nano-size of the crystals, the ion release experiments of Chen *et al.* were conducted in saline media only. Conversely, in this study, zeolites were immersed in protein-rich media (due to FBS supplementation) whose adsorption onto the zeolite mesopores or on the outer surface may hinder the mobility of species contained inside the pores and channels. This was highlighted by Bingre *et al.*⁴⁴ who established a relationship between structural features of ZSM-5 crystals and the diffusivity of probe molecules. Furthermore, Titus *et al.*⁴⁵ already found that protein monomers (*i.e.* amino acids) could strongly adsorb on ZSM-5 zeolites by hydrophobic interactions. Manifold proteins can form a “corona” on FAU nanocrystals including apolipoprotein, fibrinogen, or even albumin.⁴⁶ Vinu and co-workers⁴⁷ showed that mesoporous silicas (MCM-41 and SBA-15) displayed a strong affinity toward one of the heme proteins, and this adsorptive ability was further increased upon the introduction of aluminum atoms into the framework, which further reinforced the electrostatic interactions arising from the net negative charge harbored by aluminum atoms. According to this, it is worth mentioning here that as observed in Fig. 3(b) and (d), Mg²⁺ and Ca²⁺ concentrations remained fairly constant within the first 24 h. Between the first point taken after 0.5 h and after 24 h of the experiment, the concentrations of Mg²⁺

Table 1 Textural properties of Ca-Y and Mg-Y

Sample	BET surface area (m ² g ⁻¹)	Micropore surface area (m ² g ⁻¹)	Total pore volume (cm ³ g ⁻¹)	Micropore volume (cm ³ g ⁻¹)	Average pore diameter (nm)
Ca-Y	599	524	0.35	0.26	2.3
Mg-Y	618	539	0.36	0.26	2.3



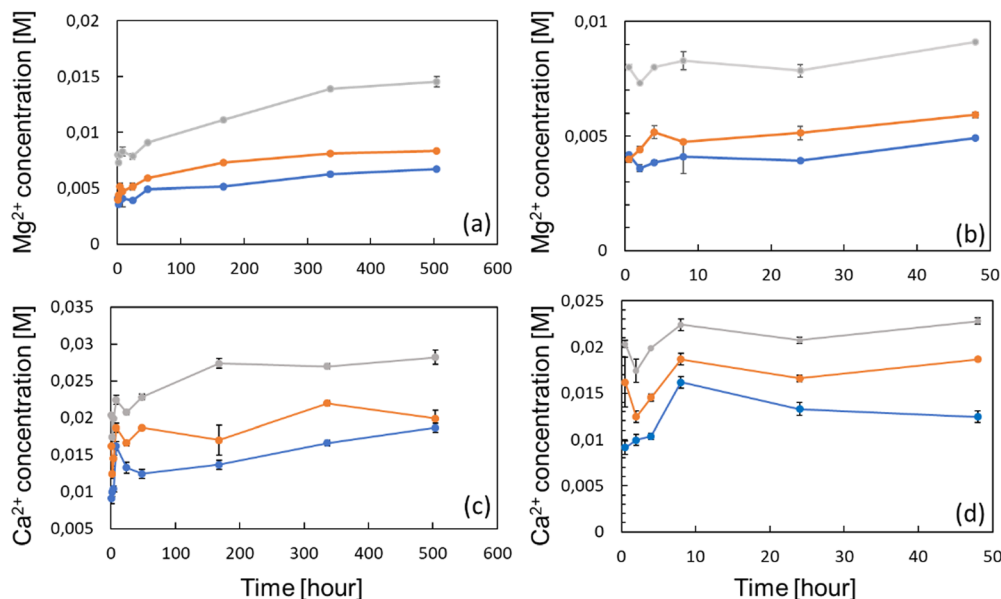


Fig. 3 Global release profiles of Mg^{2+} ions from FAU zeolites from 0.5 to 504 h (a), and the corresponding profiles of Ca^{2+} ions (c). Same profiles focused on the first 48 h for (b) Mg^{2+} ions and (d) Ca^{2+} ions. Three zeolite concentrations were used, namely 1 wt% (blue), 1.5 wt% (orange), and 3 wt% (gray). The values are represented as mean SD, $n = 3$.

varied from 4.1 to 3.9 mM (Mg 1%), from 3.1 to 5.9 mM (Mg 1.5%) and from 7.9 to 7.8 mM (Mg 3%). The Mg basal concentration of the complete α -MEM solely was found to be around 1.0 mM, indicating that, for all experimental points, the Mg concentration was higher and above the detection threshold. Similarly, the Ca^{2+} concentration of the bare complete medium was 1.3 mM, below the smallest values found under all zeolite-exposed conditions. For Mg, the Ca variation within the first 24 h was anecdotal except for Ca 1% whose value increased from 9.1 to 13.2 mM; conversely, the two other cases displayed Ca^{2+} concentration variations from 16.1 to 16.5 mM for Ca 1.5%, and from 20.3 to 20.7 mM for Ca 3%.

The viability/proliferation of MC3T3-E1 pre-osteoblastic cells was assessed using the reduction of resazurin assay (*i.e.* Alamarblue™) and the results are shown in Fig. 4(a). The reduction percentages were normalized with respect to the results of day 3, in order to emphasize the proliferation in each condition. On the one hand, one can see that the proliferation of a positive control (Ctrl+) was not very pronounced, with only a slight increase of the average relative reduction percentage (0.84 to 1.04) between days 7 and 21, which was not found to be statistically significant. On the other hand, the proliferation of Mg- or Ca-exposed cells was more important especially between days 7 and 14, prior to stabilization. Globally, cells continuously proliferated from days 7 to 21 except for Ca 1% whose average normalized intensity values decreased from 1.60 to 1.15. Also, the proliferation of cells exposed to Mg 3% was slightly less at days 14 and 21 compared to Mg 1% and Mg 1.5% even though it was not found statistically different.

The ion concentrations during culture experiments were measured using capillary electrophoresis (Fig. 4(b)); since the culture media were changed upon viability/proliferation assays,

some ions were inevitably removed. The Mg^{2+} levels remained stable between days 7 and 14 under all conditions which indicates that the cation release kinetics over 7 days is conserved, but also that zeolites are suitable for their sustainable delivery over time. At day 21, the cation concentration decreased for all samples, likely because most of the cations adsorbed onto the zeolite surface were released. Conversely, the Ca^{2+} levels were increased from day 7 to day 14 in Ca 1% and Ca 3% samples. The measured concentrations were higher than that for Mg^{2+} especially at day 14, with values of 14.4 ± 1 mM (Ca 1%), 13.9 ± 1 mM (Ca 1.5%) and 19.6 ± 0.4 mM (Ca 3%), which were in line with the higher payload of Ca^{2+} cations in FAU displayed on N_2 adsorption-desorption isotherms (Fig. 2(a) and Table 1).

For Mg 1%, the ion molarities increased from 7.3 ± 1.5 mM to 7.6 ± 2.0 mM between days 7 and 14, and decreased to 2.5 ± 0.2 mM at day 21. In the case of Mg 1.5%, the concentration increased from 9.5 ± 2 mM to 13 ± 3 mM between days 7 and 14, and varied from 13 ± 2 to 9.0 ± 0.4 mM for the last sample (Mg 3%) during the same time interval. According to Fig. 4(a), one can conclude that the proliferation of osteoblasts with Mg 3% was less pronounced than that with other conditions, albeit normalized intensities were close to that of Mg 1.5%. Wu and co-workers⁴⁸ found that alkaline phosphatase (ALP) and tartrate-resistant acid phosphatase (TRAP) activities were decreased in osteoblasts incubated with Mg extracts above 14 mM, while the highest activity was measured between 3 and 10 mM at the same time-points. It is possible that an upper limit was reached and maintained for longer periods in Mg 3% samples, thus explaining this reduction. In contrast, Shen *et al.*⁴⁹ claimed that, for MC3T3-E1 cells, the most appropriate concentration of Mg^{2+} ions was around 4.1 mM, and, above this



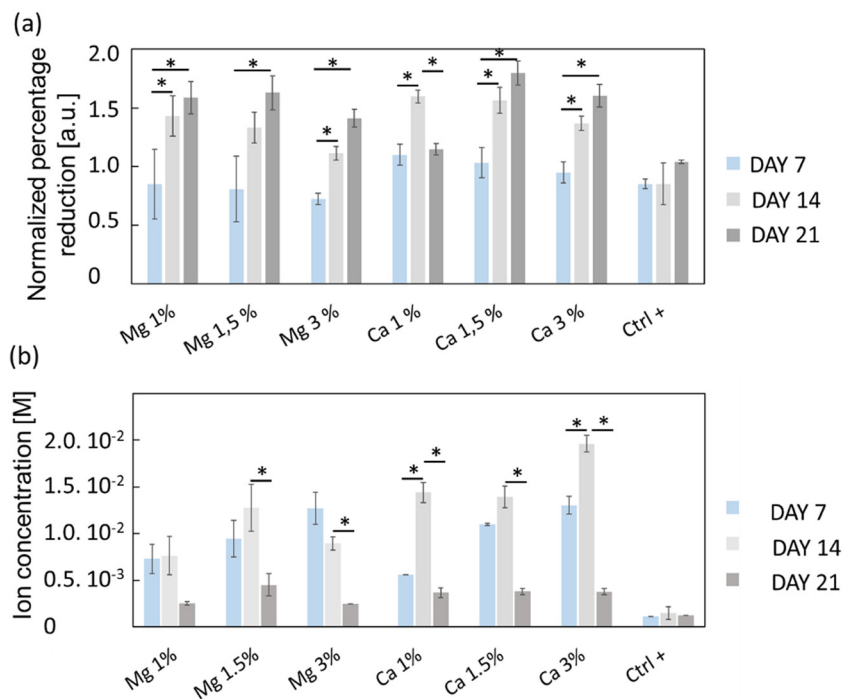


Fig. 4 (a) Proliferative activity of MC3T3-E1 osteoblasts evaluated from the reduction percentage of resazurin (AlamarBlue[®]) over 21 days for both Mg-exchanged FAU (Mg 1%, Mg 1.5% and Mg 3%) and Ca-exchanged FAU (Ca 1%, Ca 1.5% and Ca 3%), and control conditions (Ctrl+) consisting of cell culture directly onto glass coverslips without zeolites. (b) Mg and Ca concentrations collected from culture media and measured by capillary electrophoresis. For each condition, $n = 4$ and the values are represented as mean \pm SD. * for $p < 0.05$.

value, adhesion, proliferation and migration regressed, whereas in our case the cell proliferation was the highest for Mg 1% and Mg 1.5% despite the corresponding maximal concentrations of 7.6 and 13 mM, respectively. In this study, the concentrations evolved due to the progressive release of cations from the zeolites, but also by the necessary changes of culture media. Thus, the concentrations measured at specific time points do not represent a constant value but must be rather smoothed, and according to the release profiles (Fig. 3), Mg concentrations reached 4 mM before 10 h for both Mg 1% and Mg 1.5% which indicates that MC3T3-E1 proliferation can be induced at larger ranges, and that the cell response may be different in time-evolutive Mg²⁺ concentrations compared to fixed concentrations, triggering some adaptative mechanisms. Of note, a 10 mM Mg content is thought to promote MC3T3-E1 binding to type I collagen through $\alpha 2\beta 1$ integrins, further stimulating proliferation and differentiation *via* the FAK/ERK signaling pathway,⁵⁰ which emphasizes the beneficial effect of a moderate (10 mM) Mg²⁺ concentration on cell responses. The slow release kinetics described herein may also avoid a Mg burst release, known to affect the pH value. Indeed, Wu *et al.*⁵¹ showed that progressive exposure to Mg²⁺ ions released from bioceramic substrates enhanced osteogenesis of MC3T3-E1 cells without pH-related damage to the cell integrity. After 7 days, the Ca²⁺ cation concentrations were fairly proportional to the mass of zeolites *i.e.* 5.6 ± 0.2 mM (Ca 1%), 11.0 ± 0.1 mM (Ca 1.5%), and 13.0 ± 1 mM (Ca 3%). Unlike Mg-loaded samples, the Ca²⁺ concentrations increased slightly after 14 days. It is therefore possible that different diffusion regimes may occur

for Ca²⁺ ions, across either micropores or mesopores. Indeed, our team was able to decipher several effective diffusion contributions of various probes in zeolites.^{44,52}

The highest values at day 14 were respectively 14.4 ± 1 mM (Ca 1%), 13.9 ± 1 (Ca 1.5%) and 19.6 ± 0.1 mM (Ca 3%). The effectiveness of Ca²⁺ ions to trigger the proliferation of osteoblastic cells *via* the activation of the calcium-sensing receptor (CaSR) was demonstrated by Hu *et al.*⁵³ whereby the highest cell number was obtained for extracellular calcium concentrations of 5 and 10 mM. Cytotoxic effects were assigned to a Ca²⁺ concentration above 10 mM in mouse primary osteoblasts.⁵⁴ In another study, Gabusi *et al.*⁵⁵ found that the proliferation of human osteoblasts was promoted in media supplemented with 2.6 mM CaCl₂, as confirmed by ERK and phospholipase C- $\beta 1$ expression levels, but they did not probe higher concentrations. Nonetheless, Xiang *et al.*⁵⁶ showed that the migration and adhesion of osteoblasts was enhanced at lower extracellular Ca²⁺ concentration (0.5 mM), whereas the osteoblastic activities assessed through YAP/TAZ localization in the nucleus were more pronounced at 1.2 mM. Interestingly, the ability of extracellular Ca²⁺ to regulate gene expression and protein secretions was also demonstrated for MSCs, whose secretory profiles of osteopontin and transforming growth factor beta 1 (TGF- $\beta 1$) were elevated at Ca²⁺ concentrations within the range of 6–10 mM.⁵⁷ Overall, the dynamic remodeling of bones induces significant ion fluctuations whereby the Ca²⁺ concentration can increase up to 40 mM.⁵⁸ Furthermore, Ca²⁺ ions can also induce a conformational change of serum proteins such as



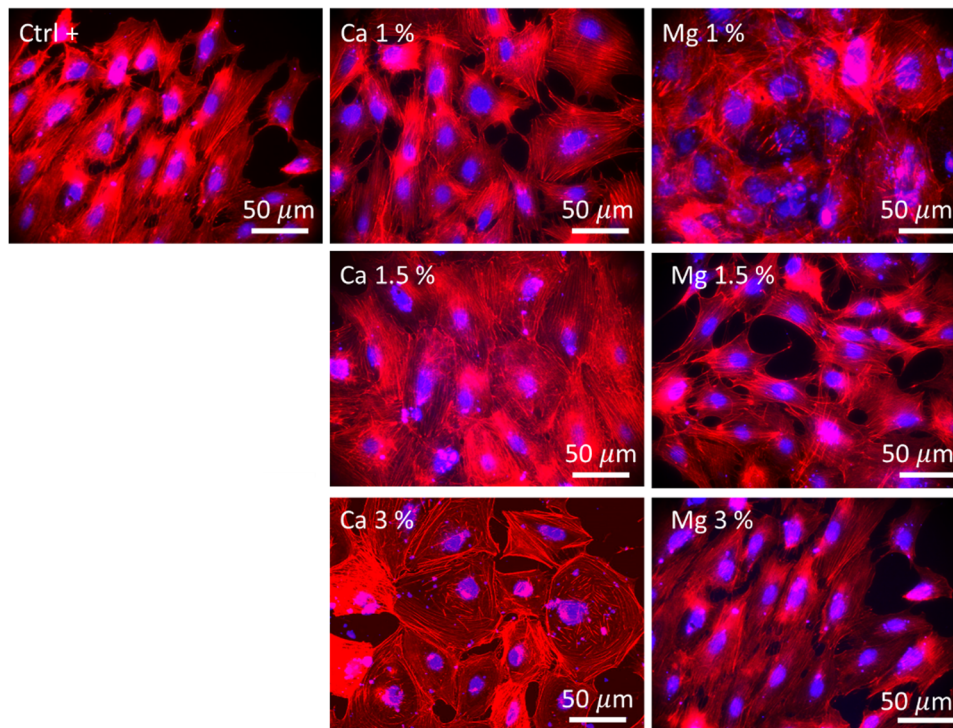


Fig. 5 Images displaying the morphologies of MC3T3-E1 cells after 21 days under an epifluorescence microscope. F-actin filaments were stained using Alexa Fluor™ 568 Phalloidin (red), and nuclei were stained using DAPI (4',6-diamidino-2-phenylindole, dihydrochloride) (blue). Ctrl+ corresponded to zeolite-free conditions. Both Mg- and Ca-loaded FAU were imaged at all zeolite concentrations.

albumin, which further modifies the binding receptors involved in cell adhesion and subsequently the related downstream signaling cascades.⁵⁹ Such ion variations can arise from several factors such as changing media, but also Ca precipitation induced by phosphate-releasing materials⁶⁰ including HAp. Atif *et al.*⁶¹ recently found that under static conditions, extracellular Ca can decrease to 0.8 mM which prevents MC3T3-E1 adhesion. In their study, they used microfluidic chips to perfuse fresh media continuously, and dampen Ca depletion. In a sense, the sustained release promoted by the presence of zeolites can also prevent the Ca decrease observed in static cultures.

The morphology of MC3T3-E1 cells was observed after 21 days of culture and in the absence of zeolites (Fig. 5, Ctrl+), whereby cells were elongated as evidenced by the longitudinal alignment of F-actin fibers, which is consistent with the actin organization on flat and moderately stiff glass coverslips.⁶² Stress fibers could be observed for Ca 1% and Mg 1% along with filopodia extensions, but without the characteristic alignment found in Ctrl+. The cell density was higher for Mg 1% compared to those for the other Mg samples. Shen *et al.*⁴⁹ showed that the surface of osteoblastic cells increases with a Mg²⁺ concentration up to 8 mM (7.6 mM found at maximum in our study) prior to diminishing which is in accordance with another recent study that depicted the same dependence of the size on Mg²⁺ ions, based on the argument that a lot of proteins, proteases, or apolipoproteins are prone to adsorb onto material surfaces in the presence of less than 10 mM Mg²⁺.⁶³ Likewise, protein adsorption may provide several sites to support cell

adhesion and the establishment of focal contacts. Moreover, MC3T3-E1 cells in Mg 1% displayed the polygonal morphology whereas they appeared smaller and spindle-shaped in Mg 1.5%. The higher Mg loading may possibly favor the extension of long protein chains (microtubules) from the centrioles in all directions. At higher Mg loading, no difference could be detected in Mg 3% with respect to Ctrl+ based on the visual aspect. It is well-known that the cell adhesion depends on the magnesium concentration, until an upper limit (~10 mM) which induces cellular damages.⁶⁴ Abed *et al.*⁶⁵ unveiled that the Mg influx in MG-63 osteoblastic cells relies on the melastatin-like transient receptor potential 7 (TRPM7), being itself regulated by the level of extracellular Mg (at concentrations higher than 0.1 mM), and subsequently, triggers cell migration and proliferation mechanisms. However, their study also suggested the prominent role of platelet-derived growth factors (PDGFs) in conjunction with TRPM7 which was not supplemented in the present work. Hence, the lack of a noticeable difference in the structural organization of actin filaments in Mg 1.5% and Mg 3% samples can be correlated to the absence of PDGF supplementation.

The highest cell population in samples with Ca²⁺ ions was found for Ca 1.5% with large flattened and cuboidal morphologies along with cell-cell contacts. This morphology was conserved in Ca 3% albeit more isolated, with lamellipodia outstretched, which either confirms the stable adhesion on the substrate,⁶⁶ or can be associated with an early commitment in osteoblastic lineage.⁶⁷ Moreover, the number of cell-cell and cell-matrix contacts is also regulated by the extracellular Ca,



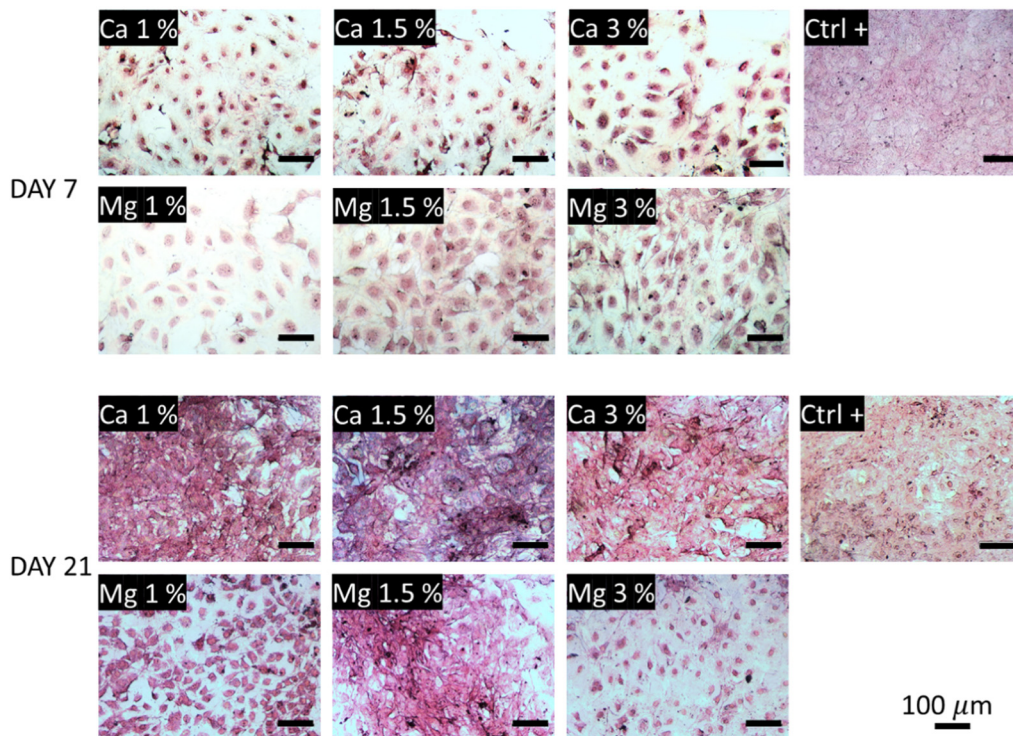


Fig. 6 Collagen secretions visualized under a light microscope after Picrosirius red staining. The collagenous content appears in pink-red color.

which was demonstrated by Nakamura *et al.*,⁶⁸ whereby, connexin43, a marker of cell-cell contacts and integrin β 1, a marker of cell-matrix contacts were both overexpressed in MC3T3 E1 cultured in 50 mM Ca compared to that in 6 mM. In this study, the largest concentrations were found to be between 14.4 and 19.6 mM (Fig. 4(b)), a range for which the Ca-dependence of the mode and the strength of adhesion is significant. As previously emphasized, it is likely that such a Ca-dependence of cell morphology and proliferation is related either to surface receptors (CaSR)⁵¹ or to G-coupled proteins such as calmodulin, which is sensitive to extracellular Ca, responsible for the Ca influx in the osteoblast cytoplasm, and in turn governs numerous cellular processes.^{66,69}

The collagen secretions were visualized under a light microscope using Picrosirius red staining. In Fig. 6, one can observe poor collagen secretions after 7 days regardless of the conditions tested compared with the control. The smallest secretions were observed in Ca 1% and Ca 1.5% samples while they were a bit more marked in Ca 3%. In comparison, higher secretions could be observed in Mg-containing conditions, with a slight increase in Mg 1.5% samples. The influence of Mg to promote ECM deposition including collagen is clearly established;⁷⁰ Liu *et al.*⁷¹ showed that ECM depositions by MC3T3-E1 were altered above 10 mM Mg. Here, these values were reached as early as at 7 days in Mg 3% (12.7 mM), which may explain the reduced collagen secretions and the associated lower proliferation (Fig. 4(a)). Of note, type I collagen is more secreted under a dual release of Cu and Mg than Mg alone.⁷² After 21 days, the trend is fully inverted, and the samples exposed to Ca^{2+} ions show a dramatic increase of protein secretions even larger than

in control samples, suggesting a delayed production of collagen by MC3T3-E1 cells in the presence of Ca^{2+} ions. No distinction could be made between all the conditions of Ca^{2+} ions at day 21. Although the influence of Ca^{2+} ions on collagen secretions was well evidenced, the optimal molarity is still unclear since the Ca^{2+} concentration is rather transient in the bone micro-environment, and Ca^{2+} levels are often evolutive owing to their release from bioceramics for instance.⁷³ Furthermore, the targeted concentration of Ca^{2+} may also vary between different cell types.⁷⁴ Likewise, early works of Valerio *et al.*⁷⁵ nuanced the correlation between the collagen deposition and Ca content in the range of 2.5–25 mM. The distinction between Mg-loaded samples was more pronounced as indicated by a moderate increase for Mg 1% between days 7 and 21, a marked deposition for Mg 1.5%, and a small decrease for Mg 3%.

5. Conclusions

In summary, this study demonstrates that nanosized FAU zeolite crystals can be used as a reservoir for the sustained delivery of bioactive cations (*i.e.* Mg^{2+} and Ca^{2+}), in a typical range of cell sensitivity, and without any cytotoxic effect. Owing to their large surface areas and adjustable pore sizes, zeolites could be investigated further as drug delivery systems considering their low cost and versatile functionalization process through ion-exchange. The ion delivery could be sustained over 21 days representative of classical cell culture experiments, and the concentrations can be adjusted by the amount of zeolites introduced in the culture medium. The prolonged release



kinetics generated an intermediate, close to *in vivo* conditions, Ca and Mg concentrations, which allowed the cell behavior to be modulated. Proliferation was the most pronounced in Mg 1% and Mg 1.5%, and for conditions with the largest amount of Ca-exchanged FAU, namely Ca 1.5% and Ca 3%. Overall, the presence of high Ca content could stimulate cell spreading and collagen secretions. In future works, zeolites could be functionalized with other types of ions to gain antimicrobial (Ag^+ or Cu^{2+}), anti-inflammatory and/or angiogenic properties. Lastly, the mesopores of zeolites could be the leverage to introduce larger molecules in their channels. Lastly, one should note that the tight cell layers observed in Fig. 5 along with the increasing density of the collagenous matrix (Fig. 6) may act as a diffusion barrier for ions or molecules trapped into zeolites underneath, as already observed for the monolayers of epithelial cells.⁷⁶ Therefore, the bioactivity of ions toward cells directly anchored to the material surface may be unaffected. Conversely, the diffusion profile of ions intended to diffuse further away from the surface (e.g. antibacterial effects) may require deeper examination, to ensure that the bioactivity of zeolite-based materials is sustained over time.

4. Materials and methods

Preparation of Mg-Y and Ca-Y zeolites

Commercial ultra-stabilized Y-zeolites (USY) were kindly supplied by Zeolyst International (CBV500) bearing ammonium ions as the charge compensation of aluminum sites ($\text{NH}_4\text{-Y}$). The ion exchange procedure was performed as follows: 1.5 g of $\text{NH}_4\text{-USY}$ were placed in a glass flask with 200 mL of magnesium chloride hexahydrate (LABOSI, 98% purity) at a concentration of 1 M. The flask was placed in a heating mantle, and then surmounted by a cooling tube. The mixture was allowed to stand at 80 °C for 2 h, and then separated by suction filtration. Afterwards, the supernatant was removed, and the ion exchange procedure was repeated twice. At the end, the resulting Mg-Y zeolites were placed in an oven at 80 °C for 48 h, and the dried powder was then used for experiments. The same procedure was used to obtain Ca-Y zeolites, except that calcium chloride dihydrate (Fluka, 99.5% purity) was mixed with 1.5 g of $\text{NH}_4\text{-Y}$ powder.

Scanning electron microscopy (SEM) and energy-dispersive X-ray spectroscopy (EDX) analyses

Scanning electron microscopy (SEM) images were acquired using a ZEISS GEMINI SEM 500 microscope at an electron high tension (EHT) voltage ranging from 2 to 6 kV. To determine the elemental distribution, EDX and mapping analyses were also performed using an EDAX SDD detector.

X-ray diffraction (XRD) analysis of Mg-USY and Ca-USY

X-ray diffraction patterns were recorded using a Bruker D8 Advance diffractometer, with a Ni detector side filtered $\text{Cu K}\alpha$ radiation (1.5406 Å) over a 2θ range of 5–65°.

Measurements of specific surface areas (BET)

The nitrogen adsorption–desorption isotherms of all zeolites were recorded at 77 K using a Micromeritics ASAP 2420. The specific surface areas and pore volumes were calculated using the Brunauer–Emmett–Teller (BET) method. Prior to analysis, FAU zeolites were pre-treated at 250 °C under vacuum for 10 h.

X-Ray fluorescence spectroscopy

Elemental analysis of the zeolites was performed by X-ray fluorescence spectroscopy using an Epsilon 3XL Panalytical apparatus. The fluorimeter holds a silver tube working at a maximum voltage of 50 kV. Samples were analyzed in the form of micrometer-sized pearls.

Cell culture

Pre-osteoblastic cells MC3T3-E1 (ATCC, subclone 4) were grown in 75 T-flasks containing α -MEM (PAN Biotech) media supplemented with 10% v/v fetal bovine serum (FBS), 1% v/v L-glutamine, and 1% v/v penicillin/streptomycin, and placed in an incubator (37 °C, 5% CO_2). Before seeding, culture media were changed every 2–3 days. When the cells reached about 80% confluency, they were washed with phosphate buffer saline (PBS), and detached with an EDTA-trypsin mixture for 5 min in an incubator (37 °C, 5% CO_2), before deactivation with an equivalent volume of fresh media. Glass coverslips ($\varnothing = 12$ mm, Thermo scientific) were placed at the bottom of each well in order to be able to extract them at the end of the experiments; these coverslips could then be readily used for observation under an epifluorescence microscope. At passage number 15, cells were seeded at a density of 10 000 cells per cm^2 at the bottom of 24 well plates with 1 mL of the fresh medium. Mg-Y and Ca-Y were introduced at different weight percentages with respect to the volume of culture media (i.e. 1 mL per well), namely: 0 (control), 1, 1.5, and 3 wt%, in sterile inserts for cell culture (0.4 μm , 12 mm in diameter, PIHP01250, MilliCell[®]), and placed into each well to allow the diffusion of ions. The well-plates were placed in an incubator, and culture media were replaced at days 7, 14, 17 and 21 in order to quantify the concentration of both Ca^{2+} and Mg^{2+} ions released from zeolites.

The viability and proliferation of the cells were measured using the Alamar blue[®] (BUF012B, Bio-rad) kit, following the instructions provided by the manufacturer. Briefly, culture media were removed and replaced with a mixture of fresh culture media supplemented with the 10% v/v Alamar blue[®] reagent, and incubated for 4 hours in the dark. Afterwards, 100 μL were pipetted in each well and transferred into a 96 well-plate prior to measurements at 570 and 600 nm using a microplate reader (Synergy 2, Biotek Instruments, Inc.). The reduction percentage of Alamar blue[®] was calculated from the absorbance values at 570 and 600 nm using the following equation:

$$\text{Percentage reduction of Alamar blue} = \frac{((O2-A1) - (O1-A2))}{((R1-N2) - (R2-N1))} \quad (1)$$



where $O1 = 80\,586$ and $O2 = 117\,216$ are the molar extinction coefficients of oxidized Alamar blue at 570 and 600 nm, respectively (values provided by the manufacturer); $R1 = 155\,617$ and $R2 = 14\,652$ are the molar extinction coefficients of reduced Alamar blue also at 570 and 600 nm. $A1$ and $A2$ are the absorbance values of the samples at 570 and 600 nm, while $N1$ and $N2$ are the absorbance values of negative controls (*i.e.* media with Alamar blue without cells). The test was performed at days 7, 14, and 21, in order to quantify the proliferative potential of each conditions.

After 21 days, experiments were stopped, and cells were washed with PBS, and fixed with 500 μL of paraformaldehyde (4% v/v in PBS) for 30 min at room temperature, prior to storing at 4 °C. In order to assess the morphology of the cells, both nuclei and F-actin filaments were stained. First, the cell membrane was permeabilized using Triton[®] X-100 (0.1% v/v) in PBS for 10 min followed by two rinsing steps for 5 min in PBS. To increase the contrast, a saturation step was performed by incubation in a solution of 1% (v/v) bovin serum albumin (BSA) in PBS for 20 min. Nucleus staining was achieved by incubation for 1 hour at RT with DAPI (4',6-diamidino-2-phenylindole, dihydrochloride) (ThermoFischer, D1306) prepared at 1/100 v/v in PBS. After two rinsing steps in PBS for 10 min, F-actin filaments were stained with Alexa Fluor[™] 568 Phalloidin (ThermoFischer, A12380) at a dilution of 1/40 v/v in PBS for 30 min at RT. Then, two more rinsing steps of 10 min each in PBS were performed, prior to storing the samples in the refrigerator at 4 °C.

The amount of collagen secreted by the cells was stained using the Picosirius Red Stain Kit (Polysciences, Inc., 24901-250), following the supplier instructions. Briefly, samples were fixed with a solution of 4% v/v paraformaldehyde (prepared in PBS) for 30 min at RT prior rinsing with distilled water. Next, samples were incubated with 200 μL per well of solution B (Picosirius Red Stain) for 60 min, and subsequently incubated in 200 μL of solution C (HCl, 1 M) for 2 min. Finally, samples were dehydrated in 70% ethanol solution for 45 min keeping 200 μL per well, and placed in a refrigerator at 4 °C until observation.

Light microscopy

Collagenous secretions were visualized under a light microscope (LEICA, DM LM/P) mounted with an HD digital microscope camera (LEICA MC170 HD). Image acquisition was performed by using the Leica Application Suite (LAS.V4.12) software. The auto colour balance tool was applied before each acquisition, and the exposition time was set at 500 ms.

Epifluorescence microscopy

The morphology of the MC3T3-E1 cells was analysed using an epifluorescence microscope (Zeiss Axio Scope A1) mounted with a digital microscope camera (LEICA MC170 HD). The glass coverslips recovered by cells after 21 days of culture were placed on microscope slides. Images were acquired using the LAS.V4.12 software, and taken each time twice with an excitation/emission wavelength of 578/600 nm for Phalloidin staining,

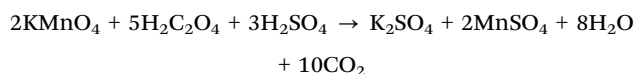
and an excitation/emission wavelength of 358/461 nm for DAPI staining (nucleus).

Capillary electrophoresis (CE)

The concentrations of both Ca^{2+} and Mg^{2+} ions released in the culture media were measured by capillary electrophoresis (Agilent CE, G1600A) at days 7, 14, 17 and 21 in accordance with viability/proliferation measurements. As the culture media were enriched with sodium ions, a 1/100 dilution of the harvested solutions was made in the background electrolytes (BEs) (*i.e.* 7 μL of culture media into 700 μL of BEs), prepared according to the methodology described by Shi *et al.*⁷⁷ Typically, imidazole (Sigma, I-0250) was prepared at 20 mM in ultrapure water, and the pH was adjusted to 6 using a solution of 3 M sulfuric acid (Fischer Scientific, S/9220/PB15). Then, hydroxypropylmethylcellulose (Merck, 09963) was dissolved at 0.1 wt%. The indirect photometric detection was used to identify ions at a wavelength of 214 nm at the cathode. The concentration of each ion was calculated after the establishment of calibration curves for concentrations ranging from 10^{-3} to 10^{-6} M (data not shown), in order to assign the corresponding retention time of each ion, while concentrations were deduced from the integrated area under each peak. The separation/quantification procedure was conducted as follows: capillary tubes (fused silica, effective length 24.5 cm, total length 33 cm, ID: 50 μm) were rinsed with a solution of 1 M sodium hydroxide for 15 min and then rinsed with BEs for 3 min. Samples were injected at a pressure of 50 mbar for 30 s, and the separation was performed at an applied tension of 10 kV for 4 min, followed by further washing steps with sodium hydroxide 1 M.

Colorimetric titrations of Ca^{2+} and Mg^{2+} ions

In conjunction with capillary electrophoresis, colorimetric titrations of Ca^{2+} and Mg^{2+} ions were also performed in order to establish the release profile of each ion over time in both ultrapure water and complete culture media. For the determination of Ca^{2+} , calibration standards were prepared using calcium chloride dihydrate (Fluka, 99.5% pure) dissolved in both ultrapure water and culture media at concentrations of 10^{-5} , 10^{-4} , 10^{-3} , 10^{-2} , 5×10^{-2} , 10^{-1} , 0.15, and 1 M, and 1 mL of these standards were then added to 4 mL of sodium oxalate solution (Fischer Scientific, BP353-500) (4 wt%) in order to form a calcium oxalate precipitate. The solutions were allowed to stand at 4 °C overnight prior to centrifugation at 10 000 rpm for 10 min. The supernatant was removed, and the calcium oxalate pellets were then dissolved in 3 M sulfuric acid at 80 °C in a heating bath. The concentration of oxalic acid was then titrated under stirring with potassium permanganate (Sigma, 223468) at 0.1 M according to the following reaction:⁷⁸



The titration end point was characterized by the appearance of a slightly pink coloration along with the brownish precipitate



due to the presence of manganese compounds. Once the calibration curve was obtained, the unknown concentration of Ca^{2+} containing samples was determined from equivalent volumes, by using the fitting curve of the calibration standards.

Regarding Mg^{2+} ions, another colorimetric titration was performed using the classical Eriochrome black T (EBT) indicator.⁷⁹ For Ca^{2+} , Mg^{2+} standards were first prepared by dissolving magnesium chloride hexahydrate (LABOSI, 98% pure) at concentrations of 10^{-4} , 10^{-3} , 10^{-2} , 10^{-1} , 0.4, 0.6, 0.8 and 1 M, in both ultrapure water and complete culture media. 1 mL of the standard solution was then mixed with 5 mL of ammonia buffer (pH = 10) *i.e.* for 100 mL, 1.07 g of ammonium chloride (Prolabo, 21236) with 6.4 mL of ammonia solution 20 wt% (Prolabo, rectapur™, 21180), and then completed up to 100 mL with ultrapure water. The whole solution was placed on a magnetic stirrer and a spatula tip containing Eriochrome Black T was added until the color turned red. Of note, as the culture media used in this study was already red due to the pH indicator, the quantity of Eriochrome Black T needed was slightly higher compared to ultrapure water. The titration was conducted with a solution of ethylenediaminetetraacetic acid (EDTA, Sigma, ED-500G) at 10^{-2} M, whilst the end point was the characteristic color shift from red to blue. At pH = 10, the Mg fixation to EBT is not selective compared to Ca-EBT complexes, and the end point of the titration corresponds to both Mg and Ca concentrations.⁸⁰ The amount of Mg ions in the culture media was determined by subtracting the basal Ca^{2+} concentration of pure media measured by capillary electrophoresis. The concentration of Mg^{2+} present in all samples was determined again by reporting the measured equivalent volumes on the calibration curve. All titrations were performed in triplicate.

Statistical analysis

All results relative to cell proliferation/viability and ion concentrations were performed in triplicate and expressed as mean \pm SD. To assess significance between different conditions, the non-parametric Mann-Whitney-Wilcoxon test was used, and conditions with p -values < 0.05 were considered as statistically different.

Author contributions

G. Lutzweiler – conceptualization, supervision, and writing; Y. Zhang – experiments and data curation; F. Gens – experiments; A. Echalar – experiments and investigation; G. Ladam – visualization; J. Hochart – investigation; T. Janicot – investigation; N. Mofaddel – supervision methodology; B. Louis – conceptualization, writing, and validation.

Conflicts of interest

There are no conflicts to declare.

Acknowledgements

The authors thank Thierry Romero for his technical assistance.

Notes and references

- 1 X. Liu, P. Chu and C. Ding, *Mater. Sci. Eng., R*, 2004, **47**, 49–121.
- 2 G. Lutzweiler, A. Ndreu Halili and N. Engin Vrana, *Pharmaceuticals*, 2020, **12**(7), 602.
- 3 A. Ho-Shui-Ling, J. Bolander, L. E. Rustom, L. A. W. Johnson, F. P. Luyten and C. Picart, *Biomaterials*, 2018, **180**, 143–162.
- 4 J. N. Zara, R. K. Siu, X. Zhang, J. Shen, R. Ngo, M. Lee, W. Li, M. Chiang, J. Chung, J. Kwak, B. M. Wu, K. Ting and C. Soo, *Tissue Eng., Part A*, 2011, **17**(9–10), 1389–1399.
- 5 N. Goonoo and A. Bhaw-Luximon, *RSC Adv.*, 2019, **9**(32), 18124–18146.
- 6 E. O'Neill, G. Awale, L. Daneshmandi, O. Umerah and K. W. H. Lo, *Drug Discovery Today*, 2018, **23**(4), 879–890.
- 7 N. J. Lakhkar, I. H. Lee, H. W. Kim, V. Salih, I. B. Wall and J. C. Knowles, *Adv. Drug Delivery Rev.*, 2013, **65**(4), 405–420.
- 8 D. W. Liu, D. C. Genetos, Y. Shao, D. J. Geist, J. L. Li, H. Z. Ke, C. H. Turner and R. L. Duncan, *Bone*, 2008, **42**, 644–652.
- 9 S. C. Yeh, J. Hou, J. W. Wu, S. Yu, Y. Zhang, K. D. Belfield, F. D. Camargo and C. P. Lin, *Nat. Commun.*, 2022, **13**(1), 1–13.
- 10 A. L. Boskey and A. S. Posner, *Mater. Res. Bull.*, 1974, **9**, 907–916.
- 11 C. C. Hung, A. Chaya, K. Liu, K. Verdelis and C. Sfeir, *Acta Biomater.*, 2019, **98**, 246–255.
- 12 T. Kokubo, M. Shigematsu, Y. Nagashima, M. Tashiro, T. Nakamura, T. Yamamuro and S. Higashi, *Bulletin of the Institute for Chemical Research*, Kyoto University, 1982, vol. 60, no. 3–4, pp. 260–268.
- 13 T. Kokubo and S. Yamaguchi, *J. Biomed. Mater. Res., Part A*, 2019, **107**(5), 968–977.
- 14 M. Bohner, B. L. G. Santoni and N. Döbelin, *Acta Biomater.*, 2020, **113**, 23–41.
- 15 Z. S. Tao, W. S. Zhou, X. W. He, W. Liu, B. L. Bai, Q. Zhou, Z. L. Huang, K. Tu, H. Li, T. Sun, Y. Lv, W. Cui and L. Yang, *Mater. Sci. Eng., C*, 2016, **62**, 226–232.
- 16 G. L. Koons, M. Diba and A. G. Mikos, *Nat. Rev. Mater.*, 2020, **5**(8), 584–603.
- 17 J. F. Navarro-González, C. Mora-Fernández and J. García-Pérez, *Seminars in Dialysis*, Blackwell Publishing Ltd, Oxford, UK, 2009, vol. 22, no. 1, pp. 37–44.
- 18 N. D. Toussaint, G. J. Elder and P. G. Kerr, *Clin. J. Am. Soc. Nephrol.*, 2009, **4**(1), 221–233.
- 19 Z. Lin, J. Wu, W. Qiao, Y. Zhao, K. H. Wong, P. K. Chu, L. Bian, S. Wu, Y. Zheng, K. M. C. Cheung, F. Leung and K. W. Yeung, *Biomaterials*, 2018, **174**, 1–16.
- 20 X. Shen, Y. Zhang, P. Ma, L. Sutrisno, Z. Luo, Y. Hu, B. Tao, C. Li and K. Cai, *Biomaterials*, 2019, **212**, 1–16.



- 21 O. Castano, N. Sachot, E. Xuriguera, E. Engel, J. A. Planell, J. H. Park, G. Z. Jin, T. H. Kim, J. H. Kim and H. W. Kim, *ACS Appl. Mater. Interfaces*, 2014, **6**(10), 7512–7522.
- 22 M. Sandomierski, M. Zielińska, K. Adamska, A. Patalas and A. Voelkel, *New J. Chem.*, 2022, **46**(7), 3401–3408.
- 23 M. A. Sakr, M. G. Mohamed, R. Wu, S. R. Shin, D. Kim, K. Kim and S. Siddiqua, *Appl. Clay Sci.*, 2020, **199**, 105860.
- 24 R. M. Barrer, *Zeolites*, 1981, **1**(3), 130–140.
- 25 C. J. Rhodes, *Sci. Prog.*, 2010, **93**(3), 223–284.
- 26 E. S. Gomes, G. Lutzweiler, P. Losch, A. V. Silva, C. Bernardon, K. Parkhomenko, M. M. Peireira and B. Louis, *Microporous Mesoporous Mater.*, 2017, **254**, 28–36.
- 27 M. M. Pereira, E. S. Gomes, A. V. Silva, A. B. Pinar, M. G. Willinger, S. Shanmugam, C. Chizallet, G. Laugel, P. Losch and B. Louis, *Chem. Sci.*, 2018, **9**(31), 6532–6539.
- 28 N. Ninan, M. Muthiah, I. K. Park, A. Elain, T. W. Wong, S. Thomas and Y. Grohens, *ACS Appl. Mater. Interfaces*, 2013, **5**(21), 11194–11206.
- 29 N. Iqbal, M. R. A. Kadir, N. H. B. Mahmood, M. F. M. Yusoff, J. A. Siddique, N. Salim, G. R. A. Froemming, M. N. Sarian, H. R. B. Baghavendran and T. Kamarul, *Ceram. Int.*, 2014, **40**(10), 16091–16097.
- 30 R. S. Bedi, D. E. Beving, L. P. Zanello and Y. Yan, *Acta Biomater.*, 2009, **5**(8), 3265–3271.
- 31 R. S. Bedi, L. P. Zanello and Y. Yan, *Adv. Funct. Mater.*, 2009, **19**(24), 3856–3861.
- 32 C. Anfray, S. Komaty, A. Corroyer-Dulmont, M. Zaarour, C. Helaine, H. Ozcelik, C. Allieux, J. Toutain, K. Goldyn, E. Petit, K. Bordji, M. Bernaudin, V. Valtchev, O. Touzani, S. Mintova and S. Valable, *Biomaterials*, 2020, **257**, 120249.
- 33 C. V. Uglea, I. Albu, A. Vatajanu, M. Croitoru, S. Antoniu, L. Panaitescu and R. M. Ottenbrite, *J. Biomater. Sci., Polym. Ed.*, 1995, **6**(7), 633–637.
- 34 X. Zhang, J. Chen, X. Pei, J. Wang, Q. Wan, S. Jiang, C. Huang and X. Pei, *ACS Appl. Mater. Interfaces*, 2017, **9**(30), 25171–25183.
- 35 S. Ivanova, B. Louis, M. J. Ledoux and C. Pham-Huu, *J. Am. Chem. Soc.*, 2007, **129**(11), 3383–3391.
- 36 B. Louis, F. Ocampo, H. S. Yun, J. P. Tessonnier and M. M. Pereira, *Chem. Eng. J.*, 2010, **161**(3), 397–402.
- 37 C. F. Imbachi-Gamba and A. L. Villa, *Mater. Today Chem.*, 2021, **20**, 100442.
- 38 R. Le Van Mao, N. T. Vu, S. Xiao and A. Ramsaran, *J. Mater. Chem.*, 1994, **4**(7), 1143–1147.
- 39 E. N. Coker and L. V. Rees, *Microporous Mesoporous Mater.*, 2005, **84**(1–3), 171–178.
- 40 C. Bernardon, B. Louis, V. Bénétou and P. Pale, *Chem-PlusChem*, 2013, **78**(9), 1134–1141.
- 41 D. W. Breck, *Zeolite molecular sieves: structure, chemistry, and use*, John Wiley & Sons, 1973.
- 42 A. Lateef, R. Nazir, N. Jamil, S. Alam, R. Shah, M. N. Khan and M. Saleem, *Microporous Mesoporous Mater.*, 2016, **232**, 174–183.
- 43 S. Chen, J. Popovich, N. Iannuzo, S. E. Haydel and D. K. Seo, *ACS Appl. Mater. Interfaces*, 2017, **9**(45), 39271–39282.
- 44 R. Bingre, P. Losch, C. Megías-Sayago, B. Vincent, P. Pale, P. Nguyen and B. Louis, *ChemPhysChem*, 2019, **20**(21), 2874–2880.
- 45 E. Titus, A. K. Kalkar and V. G. Gaikar, *Colloids Surf., A*, 2013, **223**(1–3), 55–61.
- 46 M. Rahimi, E. P. Ng, K. Bakhtiari, M. Vinciguerra, H. A. Ahmad, H. Awala, S. Mintova, M. Daghighi, F. B. Rostami, M. de Vries, M. M. Matzack, M. P. Peppelenbosch, M. Mahmoudi and F. Rezaee, *Sci. Rep.*, 2015, **5**(1), 1–12.
- 47 A. Vinu, V. Murugesan, O. Tangermann and M. Hartmann, *Chem. Mater.*, 2004, **16**(16), 3056–3065.
- 48 L. Wu, F. Feyerabend, A. F. Schilling, R. Willumeit-Römer and B. J. Luthringer, *Acta Biomater.*, 2015, **27**, 294–304.
- 49 J. Shen, B. Chen, X. Zhai, W. Qiao, S. Wu, X. Liu, Y. Zhao, C. Ruan, H. Pan, P. K. Chu, K. M. C. Cheung and K. W. Yeung, *Bioact. Mater.*, 2021, **6**(2), 503–519.
- 50 X. Nie, X. Sun, C. Wang and J. Yang, *Regener. Biomater.*, 2020, **7**(1), 53–61.
- 51 Q. Wu, S. Xu, F. Wang, B. He, X. Wang, Y. Sun, C. Ning and K. Dai, *Regener. Biomater.*, 2021, **8**(6), rbab016.
- 52 R. Bingre, B. Vincent, Q. Wang, P. Nguyen and B. Louis, *J. Phys. Chem. C*, 2028, **123**(1), 637–643.
- 53 F. Hu, L. Pan, K. Zhang, F. Xing, X. Wang, I. Lee, X. Zhang and J. Xu, *PLoS One*, 2014, **9**(9), e107217.
- 54 S. Maeno, Y. Niki, H. Matsumoto, H. Morioka, T. Yatabe, A. Funayama, Y. Tomaya, T. Tagushi and J. Tanaka, *Biomaterials*, 2005, **26**(23), 4847–4855.
- 55 E. Gabusi, C. Manferdini, F. Grassi, A. Piacentini, L. Cattini, G. Filardo, E. Lambertini, R. Piva, N. Zini, A. Facchini and G. Lisignoli, *J. Cell. Physiol.*, 2012, **227**(8), 3151–3161.
- 56 B. Xiang, Y. Liu, W. Zhao, H. Zhao and H. Yu, *Cell Biol. Int.*, 2009, **43**(10), 1125–1136.
- 57 M. N. Lee, H. S. Hwang, S. H. Oh, A. Roshanzadeh, J. W. Kim, J. H. Song, E. S. Kim and J. T. Koh, *Exp. Mol. Med.*, 2018, **50**(11), 1–16.
- 58 I. A. Silver, R. J. Murrills and D. J. Etherington, *Exp. Cell Res.*, 1988, **175**(2), 266–276.
- 59 S. L. Haag, N. R. Schiele and M. T. Bernards, *Biotechnol. Appl. Biochem.*, 2022, **69**(2), 492–502.
- 60 U. Klammert, T. Reuther, C. Jahn, B. Kraski, A. C. Kübler and U. Gbureck, *Acta Biomater.*, 2009, **5**(2), 727–734.
- 61 A. R. Atif, M. Pujari-Palmer, M. Tenje and G. Mestres, *Acta Biomater.*, 2021, **127**, 327–337.
- 62 E. Huethorst, M. F. Cutiongco, F. A. Campbell, A. Saeed, R. Love, P. M. Reynolds, M. J. Dalby and N. Gadegaard, *Biofabrication*, 2020, **12**(2), 025009.
- 63 A. Cerqueira, F. Romero-Gavilán, I. García-Arnáez, C. Martínez-Ramos, S. Ozturan, R. Izquierdo, M. Azkargorta, F. Elortza, M. Gurruchaga, J. Suay and I. Goñi, *Mater. Sci. Eng., C*, 2021, **125**, 112114.
- 64 S. Mostofi, E. Bonyadi Rad, H. Wiltsche, U. Fasching, G. Szakacs, C. Ramskogler, S. Srinivasaiah, M. Ueçal, R. Willumeit, A.-M. Weinberg and U. Schaefer, *PLoS One*, 2016, **11**(7), e0159879.
- 65 E. Abed and R. Moreau, *Am. J. Physiol.: Cell Physiol.*, 2009, **297**(2), C360–C368.



- 66 Y. Zhang, K. Wang, K. Dong, N. Cui, T. Lu and Y. Han, *Colloids Surf., B*, 2020, **187**, 110773.
- 67 N. Nabavi, Y. Urukova, M. Cardelli, J. E. Aubin and R. E. Harrison, *J. Biol. Chem.*, 2008, **283**(28), 19678–19690.
- 68 S. Nakamura, T. Matsumoto, J. I. Sasaki, H. Egusa, K. Y. Lee, T. Nakano, T. Sohmura and A. Nakahira, *Tissue Eng., Part A*, 2010, **16**(8), 2467–2473.
- 69 M. Zayzafoon, *J. Cell. Biochem.*, 2006, **97**(1), 56–70.
- 70 B. Li, Y. Han and M. Li, *J. Mater. Chem. B*, 2016, **4**(4), 683–693.
- 71 W. Liu, S. Guo, Z. Tang, X. Wei, P. Gao, N. Wang, X. Li and Z. Guo, *Biochem. Biophys. Res. Commun.*, 2020, **528**(4), 664–670.
- 72 C. Liu, X. Fu, H. Pan, P. Wan, L. Wang, L. Tan, K. Wang, Y. Zhao, K. Yang and P. K. Chu, *Sci. Rep.*, 2016, **6**(1), 1–17.
- 73 A. Nandakumar, A. Barradas, J. de Boer, L. Moroni, C. van Blitterswijk and P. Habibovic, *Biomatter*, 2013, **3**(2), e23705.
- 74 A. M. Barradas, H. A. Fernandes, N. Groen, Y. C. Chai, J. Schrooten, J. Van de Peppel, J. P. T. M. Van Leeuwen, C. A. Van Blitterswijk and J. De Boer, *Biomaterials*, 2012, **33**(11), 3205–3215.
- 75 P. Valerio, M. M. Pereira, A. M. Goes and M. F. Leite, *Biomaterials*, 2004, **25**(15), 2941–2948.
- 76 M. Mihajlovic, L. P. Van Den Heuvel, J. G. Hoenderop, J. Jansen, M. J. Wilmer, A. J. Westheim, W. A. Allebes, D. Stamatialis, L. B. Hilbrands and R. Masereeuw, *Sci. Rep.*, 2017, **7**(1), 1–14.
- 77 H. Shi, R. Zhang, G. Chandrasekher and Y. Ma, *J. Chromatogr. A*, 1994, **680**(2), 653–658.
- 78 J. C. Witt, *J. Phys. Chem.*, 2002, **26**(5), 435–446.
- 79 H. Diehl and F. Lindstrom, *Anal. Chem.*, 1959, **31**(3), 414–418.
- 80 G. P. Hildebrand and C. N. Reilley, *Anal. Chem.*, 1957, **29**(2), 258–264.

